

First-principles study of structural, electronic and magnetic properties at the (0001) Cr_2O_3 –(111) Pt interface

Marlies Reher, Nicola A. Spaldin, and Sophie F. Weber

Materials Theory, ETH Zürich, Wolfgang-Pauli-Strasse 27, 8093 Zürich, Switzerland

(Dated: May 9, 2024)

We perform first-principles density functional calculations to elucidate structural, electronic and magnetic properties at the interface of (0001) Cr_2O_3 –(111) Pt bilayers. This investigation is motivated by the fact that, despite the promise of Cr_2O_3 –Pt heterostructures in a variety of antiferromagnetic spintronic applications, many key structural, electronic, and magnetic properties at the Cr_2O_3 –Pt interface are poorly understood. We first analyze all inequivalent lateral interface alignments to determine the lowest energy interfacial structure. For all lateral alignments including the lowest-energy one, we observe an accumulation of electrons at the interface between Cr_2O_3 and Pt. We find an unexpected reversal of the magnetic moments of the interface Cr ions in the presence of Pt compared to surface Cr moments in vacuum-terminated (0001) Cr_2O_3 . We also find that the heterostructure exhibits a magnetic proximity effect in the first three Pt layers at the interface with Cr_2O_3 , providing a mechanism by which the anomalous Hall effect can occur in (0001) Cr_2O_3 –(111) Pt bilayers. Our results provide the basis for a more nuanced interpretation of magnetotransport experiments on (0001) Cr_2O_3 –(111) Pt bilayers and should inform future development of improved antiferromagnetic spintronic devices based on the Cr_2O_3 –Pt material system.

I. INTRODUCTION

Antiferromagnetic spintronic devices offer several advantages over their ferromagnetic counterparts. Due to their zero net magnetization, antiferromagnets are robust against external magnetic field perturbations, rendering them stable against data erasure [1–3]. Furthermore, the absence of a magnetic stray field for monodomain antiferromagnets allows for crosstalk-free miniaturization of bits and consequently a higher storage density [1, 4, 5]. Antiferromagnets exhibit ultrafast switching of the Néel vector, with rates in the range of THz as opposed to the GHz limit of ferromagnets [6]. Finally, antiferromagnets are more ubiquitous than ferromagnets. Therefore, the exploitation of antiferromagnets in spintronic devices vastly expands the suite of candidate materials [7].

Despite their appealing properties, a major roadblock to the widespread use of antiferromagnets in practical applications is the inherent challenge of Néel vector switching and readout arising from the vanishing bulk magnetization [1, 8]. Metallic antiferromagnets with broken time-reversal, for example CuMnAs and Mn_2Au , can be switched via electrical current pulses [3, 9]. The underlying microscopic mechanism in this case is proposed to be a relativistic spin-orbit torque. On the other hand, insulating antiferromagnets with broken time-reversal symmetry can exhibit a magnetoelectric effect (that is, an induced bulk magnetization in response to an applied electric field, or conversely an induced bulk electric polarization in response to an applied magnetic field). The Néel vector in magnetoelectric antiferromagnets can be switched via a combination of magnetic fields and electric fields [10] (instead of a current) leading to lower energy consumption. In addition, it has been shown that a rigorous symmetry correspondence exists between surface magnetization (a symmetry-allowed dipole moment per unit area) and bulk magnetoelectricity, such that anti-

ferromagnets that have a finite magnetoelectric response for an electric field along some direction \mathbf{r} also have finite surface magnetization on a surface whose normal is parallel to \mathbf{r} [11, 12]. Since the sign of this surface magnetization couples to the sign of the bulk Néel vector, the finite surface magnetization provides a direct method of readout [10–13].

Cr_2O_3 in particular is an extensively studied magnetoelectric antiferromagnet with an unusually high magnetic ordering temperature of ≈ 300 K, making it ideal for device applications [14–19]. The roughness-robust, uncompensated surface magnetization of the (0001) Cr_2O_3 surface, which has the same symmetry origin as the linear magnetoelectric response for an electric field along the [0001] direction, has been discussed theoretically [11, 12, 20] as well as experimentally [13, 21–23]. An adjacent layer of Pt can in fact be used to read out the sign of surface magnetization on (0001) Cr_2O_3 via measuring the transverse Hall voltage of Pt in response to a current applied parallel to the interface [24].

While prototype antiferromagnetic spintronic devices based on Cr_2O_3 –Pt heterostructures have been built [25], the electronic and magnetic configuration at the interface of Cr_2O_3 and Pt, as well as the detailed origin of the Hall voltage in Cr_2O_3 –Pt heterostructures are not well understood.

One effect which almost certainly contributes to the Hall voltage and its dependence on the sign of surface magnetization is the so called “Spin Hall magnetoresistance” (SMR), in which an applied in-plane electric current first generates a spin current in Pt perpendicular to the interface via the Spin Hall effect. Then, the transverse voltage in Pt generated due to the Inverse Spin Hall effect will have opposite sign depending on the sign of the Cr_2O_3 surface magnetization (and correspondingly, the sign of the Néel vector), which the spin current interacts with [26, 27].

Another possible contributing factor is the anomalous Hall effect, or AHE. The AHE, in which an electric current develops transverse to an applied current, is symmetry-forbidden in both bulk Cr_2O_3 and nonmagnetic bulk fcc Pt. Note that Cr_2O_3 in fact has broken time-reversal symmetry in the bulk, which is the minimal symmetry breaking required for the AHE, but in this case the AHE must still vanish due the product of inversion and time-reversal symmetry being preserved, although each symmetry individually is broken. However, the AHE has been reported to be present in Cr_2O_3 -Pt heterostructures [24, 28–30]. A finite Pt magnetization induced in a (0001) Cr_2O_3 -(111) Pt heterostructure via a magnetic proximity effect [24, 31] would break time-reversal symmetry in Pt, thus allowing for a nonvanishing AHE. Because the AHE and the above-described SMR, which does not require spin polarization of the Pt, both generate the same electric response, it is difficult to disentangle the contribution of the two effects experimentally. Detailed ab-initio investigations of the magnitude of induced magnetization in Pt, as well as the penetration depth, in (0001) Cr_2O_3 -(111) Pt heterostructures can help to reveal how much the AHE contributes to the Hall conductivity in Pt in magnetotransport experiments and/or spintronic devices.

Although broadly accepted that Cr_2O_3 affects the electronic, and possibly magnetic (for example, spin-polarization of Pt via magnetic proximity to Cr_2O_3) properties of Pt, there has been little to no investigation of how the magnetic and electronic properties of Cr_2O_3 are altered due to proximity to Pt. Elucidating whether Pt alters (0001) Cr_2O_3 surface magnetization is important for establishing the degree to which the magnetic properties at Cr_2O_3 vacuum- and heavy metal-terminated surfaces can be directly compared.

Based on these motivations, in this work we perform a detailed ab-initio investigation of the structural, electronic and magnetic properties at the (0001) Cr_2O_3 -(111) Pt interface. In Sec. III A we calculate the energies of all distinct high-symmetry lateral alignments of (0001) Cr_2O_3 and (111) Pt to determine the most energetically favorable lattice matching for the unreconstructed (0001) Cr_2O_3 -(111) Pt interface. In Sec. III B, we analyze the charge density distribution and layer-projected density of states for the (0001) Cr_2O_3 -(111) Pt heterostructure with the lowest energy interface. We find a significant charge redistribution due to the interaction of Cr_2O_3 and Pt, specifically, a substantial electron accumulation in the interstitial region between the Cr and Pt atoms closest to the interface. Finally, in Sec. III C, we shed light on the magnetic properties of both Cr_2O_3 and Pt near their interface, in particular, how the presence of Pt affects the Cr_2O_3 antiferromagnetic order (Subsec. III C 1), and how the proximity of boundary magnetization in Cr_2O_3 affects the spin polarization of Pt (Subsec. III C 2).

II. COMPUTATIONAL METHODS

We use density functional theory (DFT) employing the Vienna ab-initio simulation package (VASP) [32, 33] with projector-augmented-wave (PAW) pseudopotentials [33, 34]. The local spin-density approximation (LSDA) [35–39] exchange-correlation functional is combined with a Hubbard U correction (LSDA+U) [40] on the Cr d states in order to approximately account for their localized nature. We use the rotationally invariant method of Dudarev et al. [41] in which a single effective parameter U_{eff} is adjusted, as opposed to separately specifying a Hubbard U and a Hund J. We set $U_{\text{eff}} = 4$ eV based on experience from previous studies [12, 42]. The LSDA functional and the pseudopotentials Cr_{sv} , O, and Pt_{pv} with valence electrons of $\text{Cr}_{\text{sv}}:3s^23p^63d^54s^1$; $\text{O}:2s^22p^4$; and $\text{Pt}_{\text{pv}}:5p^65d^96s^1$ are chosen based on good agreement of calculated and experimental lattice parameters, see appendix. Based on our convergence tests, we choose a $7\times7\times1$ Gamma-centered k-point grid and a cutoff energy of 800 eV.

For the calculations described in the main text, we use a slab structure with six layers of Cr-terminated (0001) Cr_2O_3 , six layers of (111) Pt, and 20 Å vacuum, see Fig. 1, unless specified otherwise. Pt forms a (111) surface on (0001) Cr_2O_3 as shown in several X-ray diffraction studies [30, 43–48]. The structure files for Cr_2O_3 and Pt are obtained from the Materials Project database [49] and transformed into a slab structure using the Atomic Simulation Environment (ASE) in python [50, 51]. (111) Pt with a lattice parameter of $a=4.79$ Å is strained to (0001) Cr_2O_3 with a lattice parameter of $a=4.92$ Å, yielding a lattice mismatch of $\approx 3\%$. We fix the lattice parameters and relax the internal coordinates (while constraining the structure to maintain the original symmetry) until forces on all atoms are less than 0.01 eV/Å. During these relaxations, we fix the Cr magnetic moments to the collinear “up down up down” antiferromagnetic order with the Néel vector directed along [0001] (Fig. 1), which is known to be the ground-state order for both bulk and vacuum-terminated (0001) Cr_2O_3 [20, 42]. Given the strong spin-orbit coupling of heavy metals such as Pt, we include spin-orbit coupling self-consistently for the heterostructure relaxations, as well as all subsequent calculations described in Secs. III A, III B and III C.

III. RESULTS

A. Structural properties

First, we determine the most energetically favorable lateral alignment of the (0001) Cr_2O_3 -(111) Pt interface. An analogous ab-initio investigation of interface energetics in the isostructural heterostructure (0001) Fe_2O_3 -(111) Pt was performed in Ref. [52]. For (0001) Cr_2O_3 -(111) Pt bilayers on the other hand, the one prior DFT calculation [30] in the literature which we

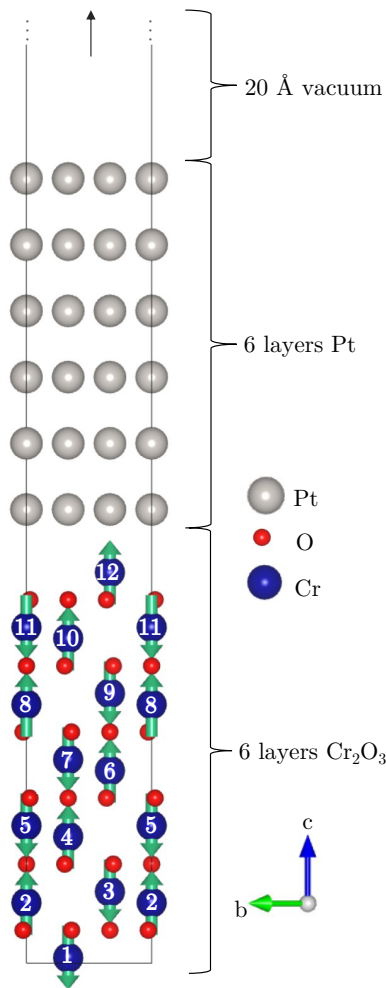


FIG. 1. The Cr_2O_3 -Pt heterostructure consisting of six Cr_2O_3 layers, six Pt layers and 20 Å of vacuum. The antiferromagnetic structure is illustrated through the corresponding magnetic moments (green arrows). The numbers on the Cr atoms show the labels used in this work. Cr12 is the interfacial Cr atom.

are aware of did not compare different lateral alignments.

Possible adsorption sites for adatoms on the (111)Pt surface are the so-called bridge, top, hollow fcc, and hollow hcp site [53] (Fig. 2). The difference between hollow fcc and hollow hcp is the presence of either a void or an atom in the second Pt layer beneath/above the adsorption site in the first Pt layer. We use this terminology to describe the lateral alignment of the interfacial Cr ion of (0001) Cr_2O_3 relative to the (111)Pt surface in the Cr_2O_3 -Pt heterostructure (Fig. 2). Two possibilities arise for the hollow fcc and hcp sites: the Pt atoms of the first Pt layer can be positioned laterally above or between the O atoms of Cr_2O_3 resulting in the four configurations hollow fcc (Pt between O), hollow hcp (Pt between O), hollow fcc (Pt on O), and hollow hcp (Pt on O) in addition to the bridge and top configuration.

We performed DFT calculations for these six lateral alignments to calculate the relaxed structure and deter-

mine the lowest energy interface configuration. Note that we were not able to converge calculations using the bridge lateral alignment. The authors of Ref. 52 mentioned the same issue for their study of (0001) Fe_2O_3 -(111)Pt heterostructures, so we suspect that the bridge alignment is highly unstable. Tab. I gives the relative energies for the five remaining lateral alignments in eV per 6-layer- Cr_2O_3 -6-layer-Pt slab (48 atoms total) used in the calculations. Note that the atomic positions for each lateral alignment are fully relaxed as described in Sec. II using the antiferromagnetic Cr_2O_3 order shown in Fig. 1. The effect of magnetic order will be studied later. The hollow hcp (Pt on O) lateral alignment exhibits the lowest energy followed by the hollow fcc (Pt on O) lateral alignment. The other lateral alignments exhibit significantly higher energies. Thus, in addition to the clear energetic preference for Cr to lie between the Pt atoms in the interfacial layer, rather than directly below (corresponding to the top lateral alignment), it is also energetically favorable for Pt to be positioned on top of the oxygen atoms.

TABLE I. Energies of different lateral alignments relative to the hollow hcp (Pt on O) lowest-energy lateral alignment.

Lateral alignment	Energy difference [eV]
Top	+0.161
Hollow hcp (Pt between O)	+0.158
Hollow fcc (Pt between O)	+0.113
Hollow fcc (Pt on O)	+0.026
Hollow hcp (Pt on O)	0.00

The energy differences of the order of 0.01 to 0.1 eV per unit cell (Tab.I) are significantly larger than the resolution of our calculations ($\approx 10^{-6}$ eV), thus we can be confident that the hollow hcp (Pt on O) lateral alignment is the most energetically stable at 0 K. Thus, for the remainder of the main text we focus on the electronic and magnetic properties of (0001) Cr_2O_3 -(111)Pt heterostructures with the hollow hcp (Pt on O) alignment (the results for other lateral alignments, given in the appendix, are qualitatively similar).

Note that at room temperature (298 K), the thermal energy $k_B T = 0.0257$ eV is close to the energy difference between hollow hcp (Pt on O) and hollow fcc (Pt on O). Thus, at the growth temperature it is possible that the two lateral alignments coexist, or hollow fcc (Pt on O) could even dominate. However, at lower temperatures closer to the 0-kelvin DFT limit, we expect only the hollow hcp (Pt on O) alignment to be stable.

Before moving on to the electronic properties, we stress that in this work, we focus on pristine, unreconstructed interfaces and have not considered possible surface reconstructions or sources of disorder such as vacancies or interstitials. Taking such disorder into account will be an important followup study.

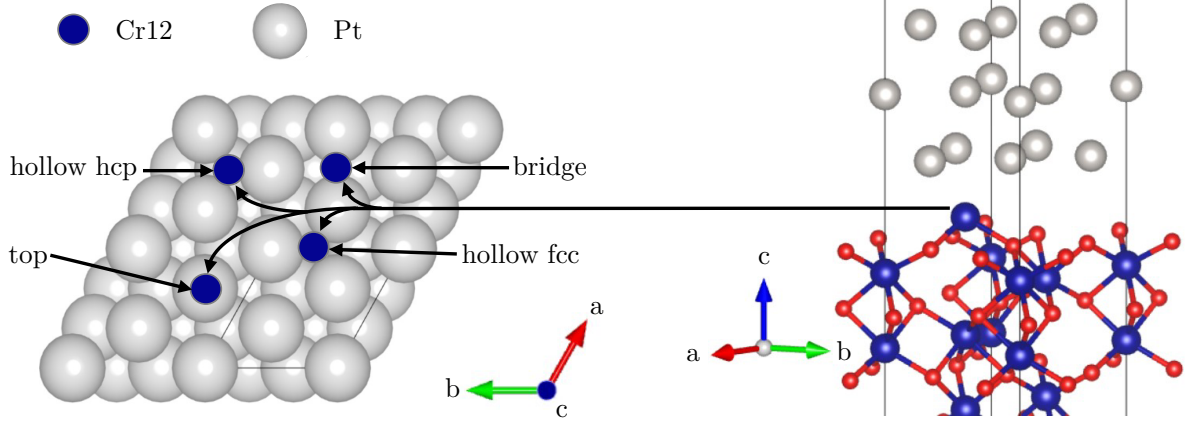


FIG. 2. Terminology to describe the lateral alignment of the (0001) Cr_2O_3 –(111)Pt interface. Left: Top view of (111)Pt surface, right: side view of hollow hcp (Pt on O) lateral alignment.

B. Electronic properties

We now analyze the electronic properties of the (0001) Cr_2O_3 –(111)Pt interface in the lowest-energy hollow hcp (Pt on O) lateral alignment. Specifically, we analyze the layer-projected density of states and calculate the real-space distribution of electronic charge using the charge density difference method.

The charge density difference $\Delta\rho$ between the charge density of the Cr_2O_3 –Pt heterostructure $\rho_{\text{Cr}_2\text{O}_3\text{--Pt}}$ and the charge density of a Cr_2O_3 slab $\rho_{\text{Cr}_2\text{O}_3}$ and a Pt slab ρ_{Pt} can be expressed as

$$\Delta\rho = \rho_{\text{Cr}_2\text{O}_3\text{--Pt}} - \rho_{\text{Cr}_2\text{O}_3} - \rho_{\text{Pt}}. \quad (1)$$

$\Delta\rho$ captures the changes in electron density, relative to the summed densities of isolated Cr_2O_3 and Pt structures, due to the mutual interaction at their interface, and is visualized with the structure visualization software VESTA in Fig. 3. While no charge transfer is visible for layers 1 to 5 in Cr_2O_3 , we observe a charge density difference in all Pt layers as well as in the layer of Cr_2O_3 at the Cr_2O_3 –Pt interface. The Pt atoms exhibit a slight depletion of electrons throughout all Pt layers, marked in blue in Fig. 3. Electrons accumulate between the Cr12 interface ion and the first Pt layer. Note that this accumulation of electrons, depicted in yellow, is present for all lateral alignments, with only the shape of the electron accumulation changing, see appendix.

The accumulation of electrons at the interface indicates a metallic behavior that is also reflected in the layer-projected density of states, shown on the right in Fig. 3. While layers 1 to 5 in Cr_2O_3 are insulating with a pronounced band gap, the interface layer (layer 6) shows a finite density of states at the Fermi energy and no clear bandgap. These effects are also robust across different alignments, see appendix.

The substantial charge accumulation between the Cr12 ions closest to the interface and the Pt directly above

already provides a qualitative hint that the properties of Cr moments at the (001) Cr_2O_3 –(111)Pt interface may be altered relative to bulk or vacuum-terminated Cr_2O_3 . This is especially evident in the Cr_2O_3 magnetism, as we will see in the next section.

C. Magnetic properties

Next, we calculate the magnetic properties of the (0001) Cr_2O_3 –(111)Pt interface to investigate whether the surface magnetization of Cr_2O_3 is affected by Pt, and whether Pt is affected by Cr_2O_3 .

1. Effect of Pt on Cr_2O_3 – Flipped magnetic moment

First, we determine how the presence of Pt in the (0001) Cr_2O_3 –(111)Pt heterostructure affects the (0001) Cr_2O_3 surface magnetization, in particular the monolayer of Cr12 moments closest to the vacuum or Pt interface. By revealing how the presence of the heavy metal modifies Cr_2O_3 magnetic properties at the interface compared to the vacuum-terminated surface, our investigation should indicate how directly magnetotransport measurements exploiting electrical readout in heavy metals can be compared with alternative experimental surface magnetization probes, such as nitrogen vacancy magnetometry.[54, 55].

We use constrained magnetic DFT as implemented by Ma and Dudarev [56] to rotate the Cr12 interface magnetic moment in steps of 45° from the bulk orientation, in which it is antiferromagnetically aligned with its nearest neighbor Cr11, to the opposite orientation. We then calculate the corresponding energies to check whether canting of the surface magnetization is energetically favorable. Without Pt (vacuum termination), the energy is lowest at 0° , that is, when the Cr_2O_3 slab retains its bulk antiferromagnetic ordering (Fig. 4). This

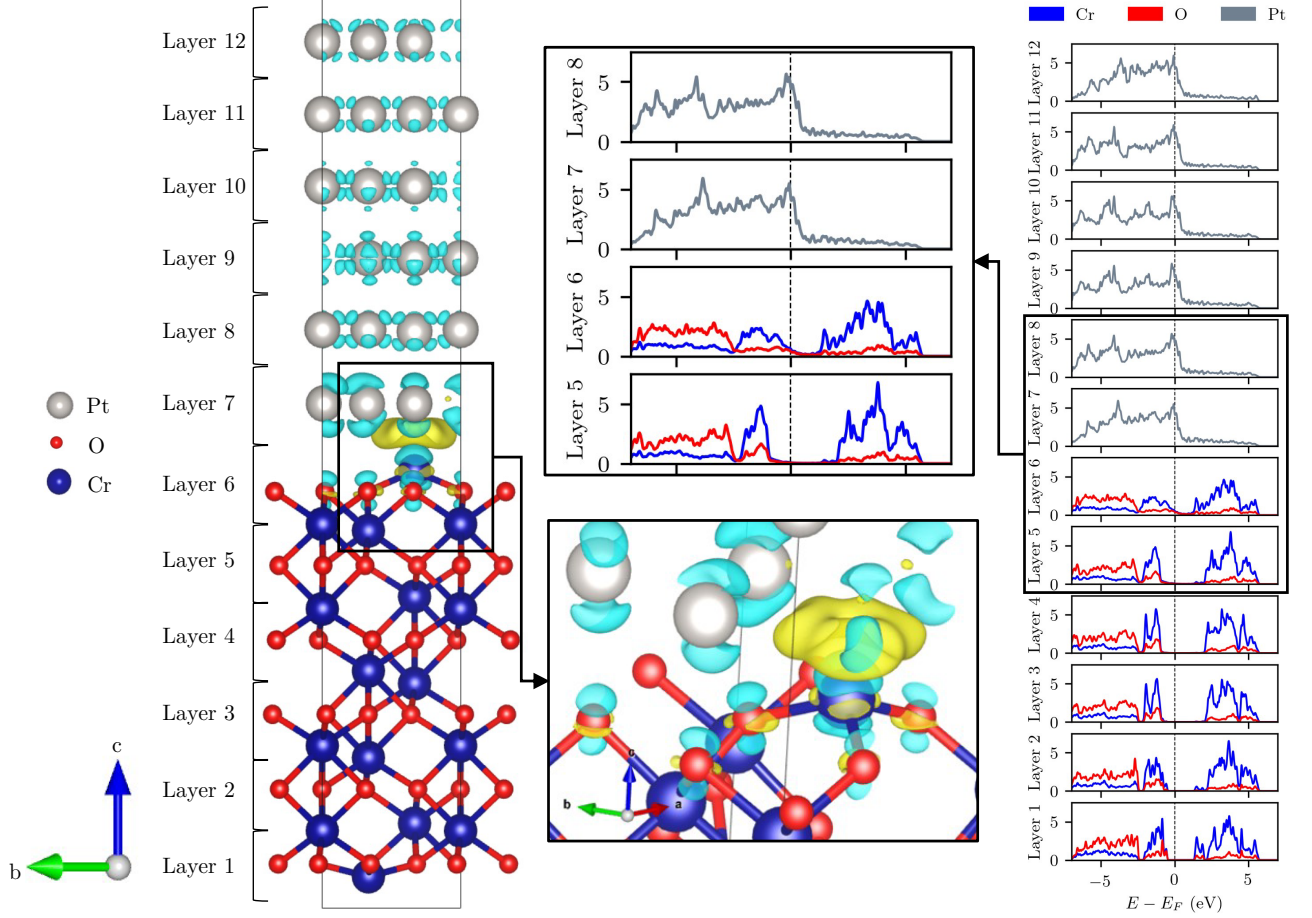


FIG. 3. Left: Calculated charge density difference for the hollow hcp (Pt on O) lateral alignment (0001)Cr₂O₃–(111)Pt heterostructure. Yellow represents an accumulation of electrons, while cyan represents a depletion of electrons. The isosurface value is set to $0.006 \frac{e}{\text{\AA}^3}$. Right: Layer-projected density of states, with the layers defined in the left-hand structure. Insets in the center zoom in on properties near the interface.

is consistent with our prior DFT studies using vacuum-terminated (0001)Cr₂O₃ [12] as well as ab-initio studies by other authors [57].

In stark contrast, for the (0001)Cr₂O₃–(111)Pt heterostructure, the energy is lowest when the magnetic moment of Cr12 is rotated by 180° (Fig. 4). This has the surprising implication that, at least for pristine, unreconstructed (0001)Cr₂O₃–(111)Pt heterostructures, the interface magnetic moment of Cr12 flips with respect to its direction in bulk and vacuum-terminated (0001)Cr₂O₃, disrupting the antiferromagnetic order at the interface and leading to a net magnetic moment in the Cr₂O₃ slab. We also confirm that the flipped Cr interface magnetic moment is energetically favorable for the four additional lateral alignments we explored in Sec. III A, see appendix. Thus, we can conclude that the reversal of (0001)Cr₂O₃ magnetization at the interface is a generic consequence of Cr₂O₃–Pt interactions, and is robust to the microscopic details of different lateral alignments. This is a key result of this work.

Exchange interactions: Next, we calculate the isotropic Heisenberg spin exchange interactions for Cr12 moments in the (0001)Cr₂O₃–(111)Pt heterostructure and compare them to those in bulk Cr₂O₃ in order to rationalize the flipping of the interface moments. We take the convention with the Heisenberg contribution to the energy given by

$$H_{\text{Heis}} = \sum_{\langle i,j \rangle} J_{ij} \hat{\mathbf{e}}_i \cdot \hat{\mathbf{e}}_j, \quad (2)$$

where J_{ij} is the Heisenberg exchange coupling parameter between magnetic moments on sites i and j , and $\hat{\mathbf{e}}_i$ is the unit vector parallel to the magnetic moment of the Cr ion at site i . Note that the convention of Eq. 2 absorbs the value of spin into the exchange constant, and thus when comparing this work's J_{ij} values to literature values where the Hamiltonian is written as $H_{\text{Heis}} = \sum_{\langle i,j \rangle} J_{ij} \mathbf{S}_i \cdot \mathbf{S}_j$, such as Ref. 42, it is necessary to divide by S^2 with S being the spin of the Cr³⁺ ion. Also, with the convention of Eq. 2, positive values

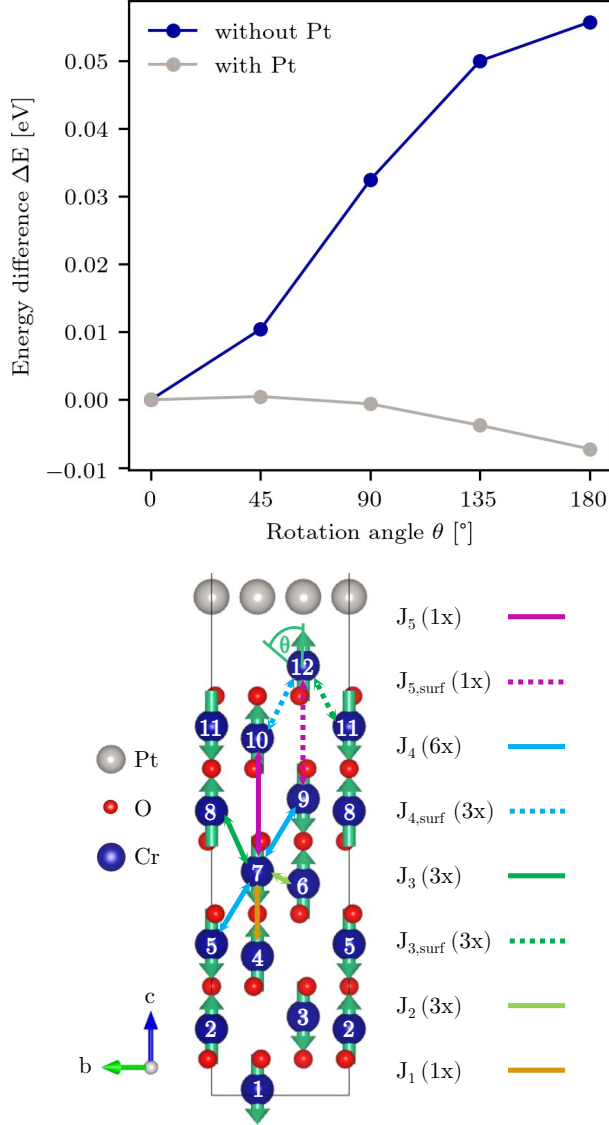


FIG. 4. Top: Energies calculated at different rotation angles (with θ defined in the bottom figure) of the Cr12 interface magnetic moment relative to the energy at 0 degrees. 0 degrees corresponds to the antiferromagnetic structure of Cr_2O_3 , while 180 degrees corresponds to Cr12 reversed (pointing downwards in this case). Bottom: Exchange interaction coupling parameters, described further in the text, for both bulk-like (Cr7) and surface/interface (Cr12) magnetic sites.

of J_{ij} indicate preferred antiferromagnetic alignment for moments i and j , whereas negative values indicate preferred ferromagnetic alignment. We use the four-state total energy method [58] whereby the exchange coupling parameter J_{ij} of the magnetic moments on atoms i and j is calculated by constraining the magnetic moments of atoms i and j to all four possible collinear configurations $\uparrow\uparrow$, $\downarrow\downarrow$, $\uparrow\downarrow$, and $\downarrow\uparrow$ while all other magnetic moments remain the same. Then

$$J_{ij} = \frac{E(\uparrow\uparrow) + E(\downarrow\downarrow) - E(\uparrow\downarrow) - E(\downarrow\uparrow)}{4N}, \quad (3)$$

with N being the coupling degeneracy (the number of symmetry-equivalent nearest neighbors corresponding to the J_{ij} of interest) and E the total DFT energy for each (ij) configuration [42, 58].

There are five relevant exchange interaction coupling parameters J_1 to J_5 for bulk Cr_2O_3 , with J_n denoting the n th nearest neighbor. Couplings beyond J_5 can be safely neglected [42]. At the Cr-terminated surface of Cr_2O_3 , the dominating, antiferromagnetic J_1 and J_2 interactions are cut off and only $J_{3,\text{surf}}$ to $J_{5,\text{surf}}$ are retained, as illustrated in Fig. 4. As a result, Cr12 in vacuum-terminated (0001) Cr_2O_3 is only weakly coupled to other Cr moments, and consequently the surface magnetization is effectively paramagnetic at room temperature, even though the bulk Néel vector is magnetically ordered [12].

We first calculate the Heisenberg exchange parameters for a Cr site in the center of the Cr_2O_3 slab (specifically Cr7, Fig. 4) to see whether Pt affects the magnetic structure far from the interface. The values (we show only J_1 and J_2 in Tab. II as these are the dominant couplings in bulk) are very close to our previous findings in bulk Cr_2O_3 see Tab. II. Consequently, we can be confident that the heterostructure we use in our DFT calculations is sufficiently thick to reproduce bulk-like behavior of Cr_2O_3 in the middle of the slab (this is also reflected in the layer-projected density of states in Fig. 3 in Sec. IIIB).

In contrast, the surface exchange parameters for the interface Cr12 are strongly affected by the presence of Pt. The most significant change with respect to the values in a relaxed vacuum-terminated slab of (0001) Cr_2O_3 (Tab. II, Ref. [12]) is for $J_{3,\text{surf}}$, which increases by more than a factor of 20 in the heterostructure and becomes ferromagnetic. This indicates a preference for Cr12 and the Cr11 just below to align parallel, consistent with the observed energy lowering in Fig. 4 for flipping Cr12 with respect to the antiferromagnetic order. $J_{4,\text{surf}}$ ($J_{5,\text{surf}}$) on the other hand favor ferromagnetic (antiferromagnetic) alignment between Cr12 and Cr10 (Cr 9), both of which favor the normal orientation $\theta = 0$ for Cr12. However, by calculating the contribution to the Heisenberg energy if Cr12 is flipped, based on Eq. 2 and the coupling degeneracies in Tab. II, we obtain

$$H_{\text{Heis}}^{\text{Cr12,flipped}} = 3J_{3,\text{surf}} - 3J_{4,\text{surf}} + J_{5,\text{surf}} = -2.2\text{meV}. \quad (4)$$

Thus, the flipping of the top layer next to the (0001) Cr_2O_3 –(111) Pt interfaces is overall energetically favorable due to the strong ferromagnetic $J_{3,\text{surf}}$ in the presence of Pt [59].

Note however, that the magnitude ~ 2 meV of the effective coupling for Cr12 in the (0001) Cr_2O_3 –(111) Pt

bilayer is very similar to the magnitude of effective coupling for Cr12 with vacuum termination[12]. Thus, we would expect Cr12 to also be effectively paramagnetic near the bulk Néel temperature in the presence of Pt. The key difference is that at low temperature where Cr12 is ordered, the interaction with Pt flips the effective coupling, and hence the ground-state direction of Cr12, with respect to the vacuum-terminated case.

TABLE II. Exchange parameters J_n in bulk Cr_2O_3 , the (0001) Cr_2O_3 –(111)Pt bilayer with hollow hcp (Pt on O) lateral alignment, and a relaxed vacuum-terminated (0001) Cr_2O_3 slab as calculated in Ref. [12]. N indicates the coupling degeneracy. Negative values of J indicate ferromagnetic couplings, and positive values refer to antiferromagnetic couplings. (Note that in Ref. [12] we used a different convention for the Heisenberg Hamiltonian such that all reported values were divided by two and multiplied by minus one relative to this table.)

J_n	N	bulk Cr_2O_3 [12] J [meV]	Cr_2O_3 –Pt J [meV]	Cr_2O_3 –vac. [12] J [meV]
J_1	1	20.92	21.10	–
J_2	3	15.76	15.98	–
$J_{3,surf}$	3	–	-10.50	0.30
$J_{4,surf}$	3	–	-9.01	-8.88
$J_{5,surf}$	1	–	2.20	0.78

2. Effect of Cr_2O_3 on Pt – Magnetic proximity effect

Finally, we briefly investigate the influence of antiferromagnetic Cr_2O_3 on Pt. A spin polarization of Pt induced via proximity to Cr_2O_3 , that is a magnetic proximity effect is a-priori likely, considering that Pt is close to the Stoner criterion. Our DFT calculations reveal a sizeable magnetization of the order of $\pm 0.01 \mu_B$ per atom in the first three Pt atomic layers at the interface with Cr_2O_3 (Fig. 5). Although Pt is strained to Cr_2O_3 , magnetization caused by strain can be excluded, as a calculation of a Pt slab strained to match the Cr_2O_3 lattice constant gives zero magnetization in Pt without the presence of Cr_2O_3 . From the fourth layer onward, the magnetization becomes negligible, dropping down to the order of $\pm 0.001 \mu_B$. We find that the Pt magnetic polarization is confined to the first three layers at the interface in all other lateral alignments as well, see appendix. Thus, based on our calculations, Pt in (0001) Cr_2O_3 –(111)Pt heterostructures exhibits a clear and localized magnetic proximity effect (MPE).

Moreover, the magnetization in Pt is inherently coupled to the antiferromagnetic domain state of Cr_2O_3 . When the domain state of Cr_2O_3 is switched (Domain A \rightarrow Domain B), the magnetization values in Pt have the same magnitude but the opposite sign (Fig. 5). The coupling of Pt to the Cr interface magnetic moment, Cr12, is antiferromagnetic for all three Pt layers with significant spin polarization with, interestingly, the maximum spin

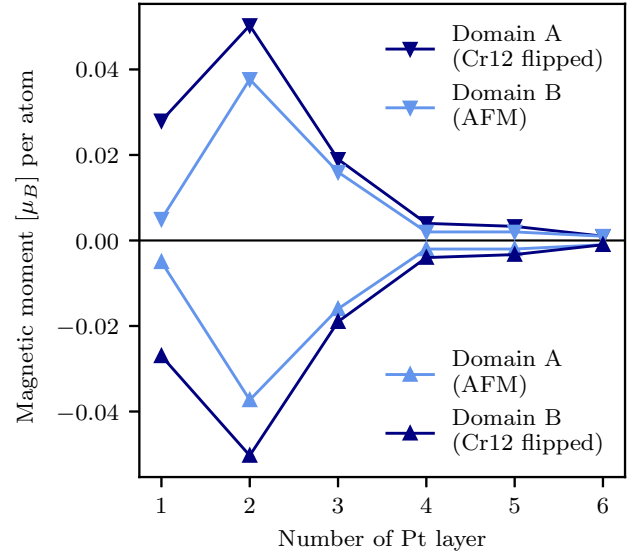


FIG. 5. Magnetization in Pt for the two different domain states in Cr_2O_3 for the antiferromagnetic configuration and the configuration with Cr12 flipped interface magnetic moment. Layer 1 is located towards Cr_2O_3 and layer 6 towards vacuum. A magnetic proximity effect is present in the first three Pt layers and changes sign when the Cr12 magnetic moment is flipped.

polarization occurring in the second Pt layer from the Cr_2O_3 –Pt interface, rather than in the Pt layer directly adjacent to Cr_2O_3 .

Lastly, related to the prior section III C 1 in which we found that for a given domain, the interface Cr12 moments flip with respect to their standard antiferromagnetic order, we also investigate the effect on spin polarization in Pt when Cr12 has the flipped ($\theta = 180^\circ$), rather than antiferromagnetic ($\theta = 0^\circ$) orientation. Importantly for experimental implications, from the dark blue lines in Fig. 5 we see that flipping the Cr12 magnetic moment into its lowest energy configuration has a similar effect on Pt as switching the domain state of Cr_2O_3 . In addition, the Cr_2O_3 –Pt interface with flipped Cr interface magnetic moment has an enhanced magnetic proximity effect in the first two Pt layers compared to the Cr_2O_3 –Pt interface with antiferromagnetic order in Cr_2O_3 .

IV. DISCUSSION AND CONCLUSIONS

In summary, we have carried out an in-depth computational exploration of the interface energetics, and the electronic and magnetic properties of (0001) Cr_2O_3 –(111)Pt heterostructures.

Our analysis of all possible pristine lateral alignments shows that interface stackings (both fcc and hcp) with Pt directly on top of O are both very close in energy to

each other, as well as being substantially lower in energy than all other lateral alignments. This finding indicates that the position of Pt relative to O is more relevant in the heterostructure energetics than whether the alignment is hollow hcp or hollow fcc. We also stress again, that the experimental relevance of our findings on lateral alignment stability must be explored further in followup studies by taking into account likely possibilities of surface reconstruction and other disorder.

Our calculations for the lowest-energy hollow hcp (Pt on O) alignment indicate substantial electronic and magnetic effects due to Cr_2O_3 -Pt interactions in the layers closest to the interface. Beyond the interface region of one Cr_2O_3 layer and three Pt layers, both Pt and Cr_2O_3 are bulklike.

One of our most potentially consequential findings is that a reversed Cr interface magnetic moment in (0001) Cr_2O_3 -(111) Pt heterostructures is energetically more favorable than the usual antiferromagnetic structure of Cr_2O_3 . This is reflected also in our calculation of the Heisenberg coupling constants for the interface Cr, in particular, a strongly ferromagnetic $J_{3,\text{surf}}$ which favors a flipping of the interface Cr compared to its alignment in the bulk or with vacuum termination. The microscopic mechanism of this flipping needs to be investigated further. Qualitatively, it is presumably tied to the observed accumulation of charge density between Cr and Pt interface moments.

Our finding of the flipping of interface Cr for (0001) Cr_2O_3 -(111) Pt heterostructures suggests that heavy metals cannot be assumed to be passive read-out elements for surface magnetic properties, but rather, their presence can drastically alter the magnetism at the surface. For (0001) Cr_2O_3 -(111) Pt heterostructures in particular, our findings (Fig. 5) reveal that a given antiferromagnetic domain with the vacuum-terminated (0001) Cr_2O_3 surface moment orientation produces a qualitatively identical response in Pt as the opposite (0001) Cr_2O_3 domain with the flipped interface moment orientation. Thus, it is important to verify whether for example established field-cooling procedures are actually switching bulk Cr_2O_3 domains, or simply switching the interface Cr with a fixed bulk domain.

Additionally, we find a substantial magnetization $\sim 0.01\mu_B$ in the first three layers of Pt induced via Cr_2O_3 . This calculated magnetic proximity effect is consistent with experiments utilizing the magneto-optical Kerr effect (MOKE) measurements [31], though it must be emphasized that spurious signals in Kerr and soft x-ray measurements can arise due to dirty samples and be confused with magnetic signals from a pure sample. In contrast, other measurements using x-ray magnetic circular dichroism (XMCD) do not find a significant MPE in (0001) Cr_2O_3 -(111) Pt heterostructures [30]. We hope our work motivates experimentalists to look more closely into the possible spin polarization of Pt, which via breaking of time-reversal symmetry would allow the AHE in Pt on (0001) Cr_2O_3 .

If an MPE in Pt for (0001) Cr_2O_3 -(111) Pt exists, an interesting experiment to test whether it contributes substantial at low temperatures to the transverse voltage signal is to compare Pt electrical resistance at depths within and beyond three layers from the interface. Based on the apparent penetration depth of the MPE, the electrical response within the first three layers of Pt should contain an additional component due to the AHE induced by the magnetized Pt. This will disappear in deeper regions of the Pt as the MPE falls off.

To conclude, our first-principles investigation of structural, electronic and magnetic properties of (0001) Cr_2O_3 -(111) Pt heterostructures can help with interpretation of magnetotransport experiments in assessing the sign of the Néel vector, as well as provide guidance in the future design of AFM spintronic devices. We also hope that our work inspires further investigation, both theoretical and experimental, of how the interactions of antiferromagnetic and heavy metal materials can lead to unexpected electric and magnetic phenomena at their interfaces.

ACKNOWLEDGMENTS

We thank Denys Makarov and Oleksandr Pylypovskiy for useful discussions. This work was funded by the ERC under the European Union's Horizon 2020 research and innovation programme with grant No. 810451, and by ETH Zürich. Computational resources were provided by ETH Zürich's EULER cluster.

APPENDIX

Appendix A: DFT Details: Assessment of functionals

We relaxed the lattice parameters of bulk Pt and bulk Cr_2O_3 with different DFT functionals and compared them to experimental values to determine the functional that best describes the Cr_2O_3 -Pt heterostructure. Tables III and IV give the values of the lattice parameters of Cr_2O_3 and Pt obtained with the local (spin) density approximation (L(S)DA) and the Perdew-Burke-Ernzerhof (PBE) functional. A Hubbard U correction is applied on the Cr 3d orbitals in both cases, as described in Sec. II. We used the VASP Cr_sv and O PAW pseudopotentials as established in previous studies [12], and compared the standard pseudopotential (Pt) and extended pseudopotential (Pt_pv) for platinum for the LDA and the PBE functional. The extended pseudopotentials ending with _pv and _sv additionally take into account semi-core p and s electrons respectively as valence electrons in addition to the usual outer shell electrons.

The results in Tables III and IV show that the LDA functional with the extended Pt_pv pseudopotential yields lattice parameters closest to the experimental

TABLE III. Relaxed lattice parameters of Cr_2O_3 computationally obtained with LDA and PBE functionals compared to the experimental value determined in Ref. [60]. Δa and Δc describe the relative difference between the computational and experimental lattice parameters.

	a [\AA]	Δa	c [\AA]	Δc
LSDA	4.9156	-0.84 %	13.5186	-0.54 %
PBE	5.0340	+1.55 %	13.8026	+1.55 %
Experiment [60]	4.9572	—	13.5917	—

TABLE IV. Relaxed lattice parameters of Pt computationally obtained with LDA and PBE functionals in combination with Pt and Pt_pv PAW pseudopotentials compared to the experimental value determined in Ref. [61]. Δa describes the relative difference between the computational and experimental lattice parameters.

	a [\AA]	Δa
LDA (Pt)	3.8326	-2.3 %
LDA (Pt_pv)	3.9096	-0.4 %
PBE (Pt)	3.9137	-0.3 %
PBE (Pt_pv)	3.9771	+1.4 %
Experiment [61]	3.9236	—

lattice parameters. Based on these results, the L(S)DA functional (+U correction) as well as Cr_sv, O, and Pt_pv pseudopotentials are selected to model the Cr_2O_3 -Pt heterostructure.

Appendix B: Electronic properties - More lateral alignments

While Sec. IIIB focuses on the electronic properties of the lowest-energy lateral alignment, here we present the electronic properties of the other lateral alignments. We find an electron accumulation in the Cr_2O_3 interface layer for all lateral alignments, with the detailed shape of the electron accumulation depending on the lateral alignment, as shown in Fig. 6. The hollow fcc and hollow hcp configurations have a triangular-shaped accumulation of electrons, with the triangle corners pointing towards the Pt atoms. The hollow fcc (Pt between O) and hollow hcp (Pt between O) lateral alignment show similar accumulations to each other; likewise the hollow fcc (Pt on O) and hollow hcp (Pt on O) alignments are similar. Consequently, the relative O-Pt position plays a larger role in the shape of the electron accumulation than whether the lateral alignment is of fcc or hcp type. The electron accumulation in the ‘top’ lateral alignment occurs in a doughnut-like shape between the Pt atom above and the Cr12 ion below. The shape of the electron accumulation stays similar upon variation of the isosurface value for all different lateral alignments. We note that the layer-projected density of states also shows a finite DOS in the Cr_2O_3 interface layer for all lateral alignments, consistent with the observed electron accumulations in Fig. 6.

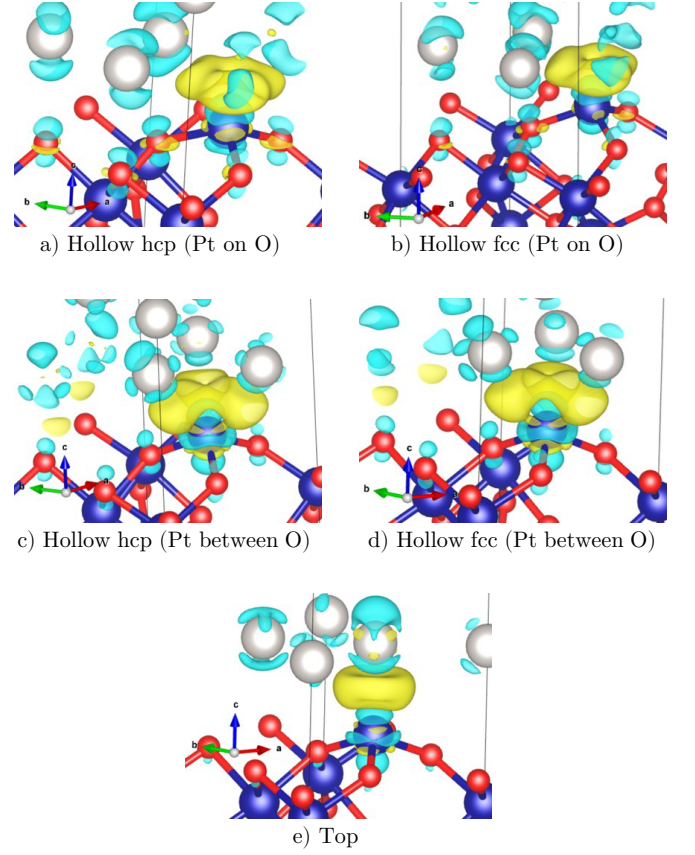


FIG. 6. Charge density differences at the interface between Cr12 and the first Pt layer for (0001) Cr_2O_3 -(111) Pt heterostructures with different lateral alignments. Yellow represents an accumulation of electrons, while cyan represents a depletion of electrons. The isosurface value in VESTA is set to $0.006 \frac{e}{\text{\AA}^3}$.

Overall, the electron accumulations appear in proximity to the Cr12 ion irrespective of whether the Cr12 magnetic moment is flipped or not, and their shape is controlled by the platinum interface lateral alignment.

Appendix C: Magnetic properties - Thicker slabs and supercell

In the main text, Cr_2O_3 -Pt heterostructures with six Cr_2O_3 layers are evaluated. In this section, the effect of an increasing number of Cr_2O_3 layers is analyzed.

The resulting energy differences between antiferromagnetic order and magnetic order with Cr12 flipped magnetic moment of four slab structures with different numbers of Cr_2O_3 layers are listed in Table V. The flipped Cr12 magnetic moment is energetically favorable for all four of them. The energy difference is similar for all four, and importantly there is no trend in increasing or decreasing energy difference that would suggest an additional thickness-dependent contribution to the energy.

In addition, we analyzed the Cr interface magnetic mo-

TABLE V. Energy difference ΔE between the flipped and antiferromagnetic Cr12 configurations for different slabs of the lowest energy lateral alignment (hollow hcp (Pt on O)) with four Pt layers.

No. Cr ₂ O ₃ layers	Energy difference ΔE [meV]
6	-18.3
7	-15.0
9	-16.1
12	-19.1

ments in a 2x1x1 supercell to check whether a combination of flipped and AFM interface Cr atoms is lower in energy than flipping all Cr moments. We found that the 2x1x1 supercell has lowest energy for both top Cr12 flipped, intermediate energy for one Cr12 flipped and one with the AFM configuration, and highest energy for both primitive magnetic cells having the bulk AFM order for the Cr12 moments. Thus, it seems that lateral spin rearrangements of Cr at the (0001) Cr₂O₃–(111) Pt which lead to a mixed flipped-AFM interface do not lower the energy compared to a uniformly flipped Cr12 layer. Moreover, the energy difference between both Cr flipped and both Cr in the bulk AFM configuration for the 2x1x1 supercell is almost exactly twice as large as the energy difference for the single magnetic unit cell used in the main text. This implies that no other energy contributions (for example, a non-negligible magnetic exchange between adjacent Cr12 moments mediated via RKKY interactions) which were absent in the primitive magnetic cell arise in the supercell containing two Cr12 moments. Thus, interactions between neighboring surface Cr moments in the heterostructure, like the case of the vacuum-terminated structure, can be safely neglected, and the observed flipping of Cr surface moments for the single magnetic unit cell should occur for all Cr12 moments at an experimental (0001) Cr₂O₃–(111) Pt interface.

Appendix D: Magnetic properties - Further analysis of MPE

Section III C 2 described the observation of a magnetic proximity effect (MPE) for a (0001) Cr₂O₃–(111) Pt heterostructure with six Pt layers in a hollow hcp (Pt on O) lateral alignment. This section analyzes the MPE of the other lateral alignments as well as its dependence on the thickness of Pt.

Fig. 7 and Fig. 8 show the calculated magnetic moment per Pt atom as a function of the Pt layer number for different lateral alignments. For all cases, the Pt magnetization points along the [0001] hexagonal direction, perpendicular to the (0001) Cr₂O₃–(111) Pt interface, with negligible in-plane components. We see that the MPE is present for all lateral alignments, and in all cases occurs in the first three Pt layers adjacent to Cr₂O₃. The hollow fcc (Pt on O) magnetization values (purple) and hollow hcp (Pt on O) magnetization values (brown) have

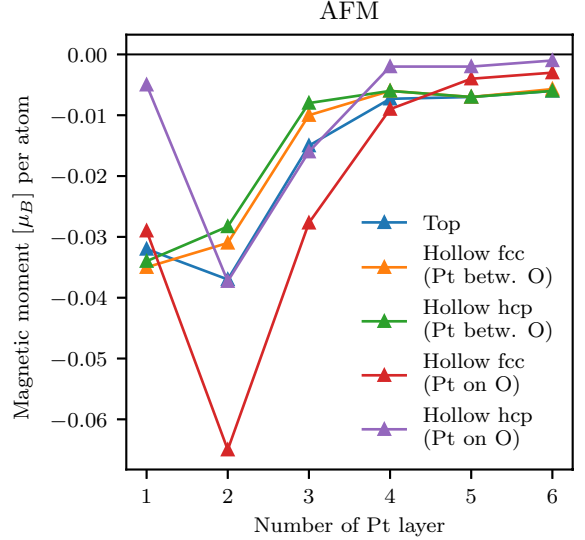


FIG. 7. Magnetization of Pt atoms in the hexagonal [0001] direction as a function of Pt layer for all different lateral alignments with antiferromagnetic order in Cr₂O₃. A magnetic proximity effect is pronounced in the first three Pt layers.

the same dependence on distance from the interface; likewise, the hollow fcc (Pt between O) values (green) and hollow hcp (Pt between O) values (red) have the same dependence. This suggests that the relative alignment of Pt and O affects the MPE more than whether the alignment is of fcc or hcp type. This is analogous to the behavior of the electron accumulation described in Sec. B.

In the main text a heterostructure with six Pt layers was analyzed. Here, we vary the number of Pt layers to see whether the MPE is affected, in particular to determine whether the thickness of the penetration depth of the MPE depends on the thickness of Pt. Fig. 9 and Fig. 10 show the magnetization in Pt for up to eight Pt layers for a heterostructure with antiferromagnetic Cr₂O₃ and a heterostructure with Cr₂O₃ with flipped Cr12 magnetic moment, respectively. Regardless of the magnetic order in Cr₂O₃ and regardless of the thickness of Pt, the MPE is pronounced only in the first three Pt layers adjacent to Cr₂O₃. As described in Sec. III C, Pt is coupled antiferromagnetically to the Cr12 interface magnetic moment and the flipped Cr12 magnetic moment increases the MPE, which explains the change in sign as well as the difference in magnitude between Fig. 9 and Fig. 10.

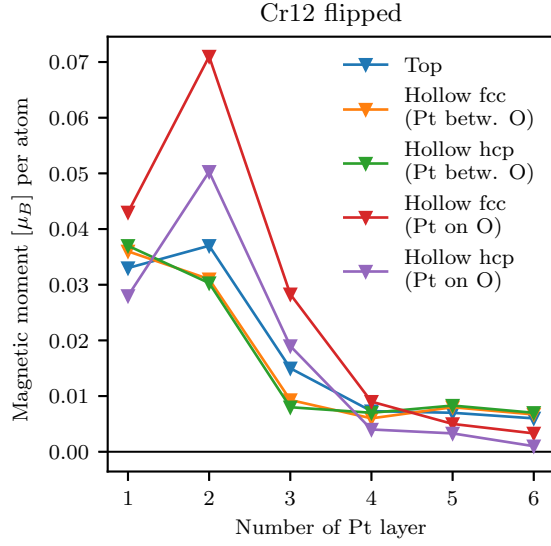


FIG. 8. Magnetization of Pt atoms in the hexagonal [0001] direction as a function of Pt layer number for different lateral alignments. The Cr_2O_3 slab has the Cr12 magnetic moment flipped, in agreement with our calculated ground state for the heterostructure. A magnetic proximity effect is pronounced in the first three Pt layers.

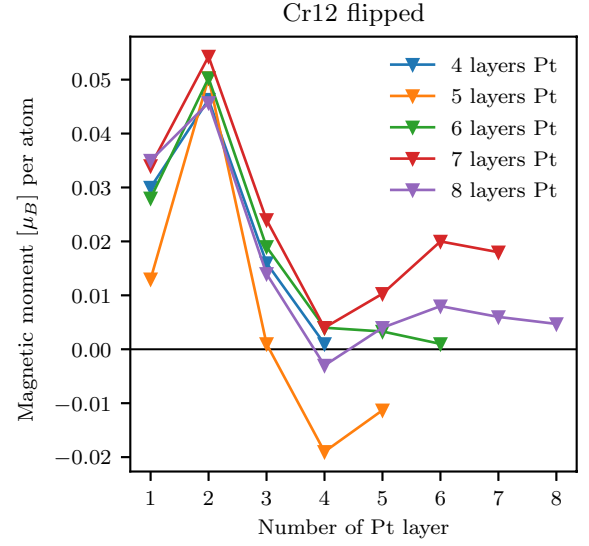


FIG. 10. Magnetization of Pt atoms in the hexagonal [0001] direction as a function of Pt layer number for different Pt layer thicknesses with flipped Cr12 magnetic moment in Cr_2O_3 . A magnetic proximity effect is pronounced in the first three Pt layers.

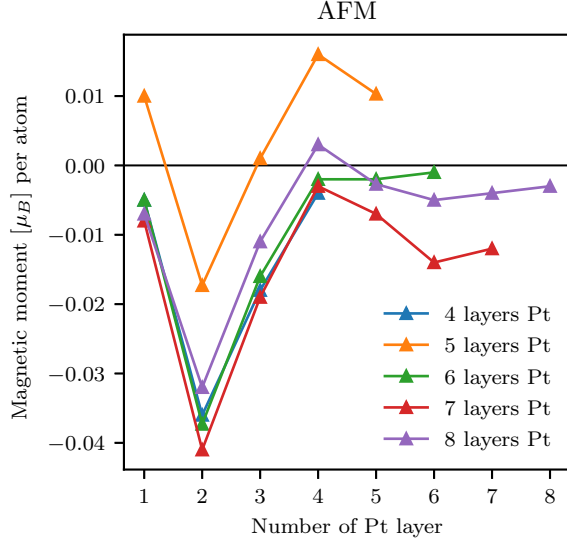


FIG. 9. Magnetization of Pt atoms in the hexagonal [0001] direction as a function of Pt layer number for different numbers of Pt layer thicknesses with antiferromagnetic order in Cr_2O_3 . A magnetic proximity effect is pronounced in the first three Pt layers.

- [1] V. Baltz, A. Manchon, M. Tsoi, T. Moriyama, T. Ono, and Y. Tserkovnyak, Antiferromagnetic spintronics, *Reviews of Modern Physics* **90**, 015005 (2018).
- [2] E. V. Gomonay and V. M. Loktev, Spintronics of antiferromagnetic systems (Review Article), *Low Temperature Physics* **40**, 17 (2014).
- [3] P. Wadley, B. Howells, J. Železný, C. Andrews, V. Hills, R. P. Campion, V. Novák, K. Olejník, F. Maccherozzi, S. S. Dhesi, S. Y. Martin, T. Wagner, J. Wunderlich, F. Freimuth, Y. Mokrousov, J. Kuneš, J. S. Chauhan, M. J. Grzybowski, A. W. Rushforth, K. W. Edmonds, B. L. Gallagher, and T. Jungwirth, Electrical switching of an antiferromagnet, *Science* **351**, 587 (2016).
- [4] J. Han, R. Cheng, L. Liu, H. Ohno, and S. Fukami, Coherent antiferromagnetic spintronics, *Nature Materials* **10.1038/s41563-023-01492-6** (2023).
- [5] H. Meer, O. Gomonay, A. Wittmann, and M. Kläui, Antiferromagnetic insulatronics: Spintronics in insulating 3d metal oxides with antiferromagnetic coupling, *Applied Physics Letters* **122**, 080502 (2023).
- [6] M. Fiebig, N. P. Duong, T. Satoh, B. B. Van Aken, K. Miyano, Y. Tomioka, and Y. Tokura, Ultrafast magnetization dynamics of antiferromagnetic compounds, *Journal of Physics D: Applied Physics* **41**, 164005 (2008).
- [7] P. Němec, M. Fiebig, T. Kampfrath, and A. V. Kimel, Antiferromagnetic opto-spintronics, *Nature Physics* **14**, 229 (2018).
- [8] Y.-H. Zhang, T.-C. Chuang, D. Qu, and S.-Y. Huang, Detection and manipulation of the antiferromagnetic Néel vector in Cr_2O_3 , *Physical Review B* **105**, 094442 (2022).
- [9] S. Y. Bodnar, L. Šmejkal, I. Turek, T. Jungwirth, O. Gomonay, J. Sinova, A. A. Sapozhnik, H.-J. Elmers, M. Kläui, and M. Jourdan, Writing and reading antiferromagnetic Mn_2Au by Néel spin-orbit torques and large anisotropic magnetoresistance, *Nature Communications* **9**, 348 (2018).
- [10] X. He, Y. Wang, N. Wu, A. N. Caruso, E. Vescovo, K. D. Belashchenko, P. A. Dowben, and C. Binek, Robust isothermal electric control of exchange bias at room temperature, *Nature Materials* **9**, 579 (2010).
- [11] K. D. Belashchenko, Equilibrium Magnetization at the Boundary of a Magnetoelectric Antiferromagnet, *Physical Review Letters* **105**, 147204 (2010).
- [12] S. F. Weber and N. A. Spaldin, Characterizing and Overcoming Surface Paramagnetism in Magnetoelectric Antiferromagnets, *Physical Review Letters* **130**, 146701 (2023).
- [13] N. Wu, X. He, A. L. Wysocki, U. Lanke, T. Komesu, K. D. Belashchenko, C. Binek, and P. A. Dowben, Imaging and Control of Surface Magnetization Domains in a Magnetoelectric Antiferromagnet, *Physical Review Letters* **106**, 087202 (2011).
- [14] I. E. Dzyaloshinskii, On the magneto-electrical effect in antiferromagnets, (1959).
- [15] Y. Shiratsuchi, K. Toyoki, and R. Nakatani, Magnetoelectric control of antiferromagnetic domain state in Cr_2O_3 thin film, *Journal of Physics: Condensed Matter* **33**, 243001 (2021).
- [16] Y. Shiratsuchi, T. V. A. Nguyen, and R. Nakatani, Magnetoelectric Control of Antiferromagnetic Domain of Cr_2O_3 Thin Film Toward Spintronic Application, *Journal of the Magnetism Society of Japan* **42**, 119 (2018).
- [17] Y. Shiratsuchi, S. Watanabe, H. Yoshida, N. Kishida, R. Nakatani, Y. Kotani, K. Toyoki, and T. Nakamura, Observation of the magnetoelectric reversal process of the antiferromagnetic domain, *Applied Physics Letters* **113**, 242404 (2018).
- [18] Y. Shiratsuchi, K. Toyoki, T. Yiran, H. Aono, and R. Nakatani, Realization of magnetoelectric effect in 50-nm-thick Cr_2O_3 thin film, *Applied Physics Express* **13**, 043003 (2020).
- [19] L. Fallarino, A. Berger, and C. Binek, Magnetic field induced switching of the antiferromagnetic order parameter in thin films of magnetoelectric chromia, *Physical Review B* **91**, 054414 (2015).
- [20] S. F. Weber, A. Urru, S. Bhowal, C. Ederer, and N. A. Spaldin, Surface Magnetization in Antiferromagnets: Classification, example materials, and relation to magnetoelectric responses (2023), arXiv:2306.06631 [cond-mat, physics:physics].
- [21] S. Cao, X. Zhang, N. Wu, A. T. N'Diaye, G. Chen, A. K. Schmid, X. Chen, W. Echtenkamp, A. Enders, C. Binek, and P. A. Dowben, Spin polarization asymmetry at the surface of chromia, *New Journal of Physics* **16**, 073021 (2014).
- [22] S. Cao, N. Wu, W. Echtenkamp, V. Lauter, H. Ambaye, T. Komesu, C. Binek, and P. A. Dowben, The surface stability of $\text{Cr}_2\text{O}_3(0001)$, *Journal of Physics: Condensed Matter* **27**, 255003 (2015).
- [23] A. Erickson, S. Q. Abbas Shah, A. Mahmood, I. Fescenko, R. Timalina, C. Binek, and A. Laraoui, Nanoscale imaging of antiferromagnetic domains in epitaxial films of Cr_2O_3 via scanning diamond magnetic probe microscopy, *RSC Advances* **13**, 178 (2023).
- [24] T. Kosub, M. Kopte, F. Radu, O. G. Schmidt, and D. Makarov, All-Electric Access to the Magnetic-Field-Invariant Magnetization of Antiferromagnets, *Physical Review Letters* **115**, 097201 (2015).
- [25] T. Kosub, M. Kopte, R. Hühne, P. Appel, B. Shields, P. Maletinsky, R. Hübner, M. O. Liedke, J. Fassbender, O. G. Schmidt, and D. Makarov, Purely antiferromagnetic magnetoelectric random access memory, *Nature Communications* **8**, 13985 (2017).
- [26] Y.-T. Chen, S. Takahashi, H. Nakayama, M. Althammer, S. T. B. Goennenwein, E. Saitoh, and G. E. W. Bauer, Theory of spin Hall magnetoresistance, *Physical Review B* **87**, 144411 (2013).
- [27] R. Schlitz, T. Kosub, A. Thomas, S. Fabretti, K. Nielsch, D. Makarov, and S. T. B. Goennenwein, Evolution of the spin hall magnetoresistance in $\text{Cr}_2\text{O}_3/\text{Pt}$ bilayers close to the Néel temperature, *Applied Physics Letters* **112**, 132401 (2018).
- [28] X. Wang, K. Toyoki, R. Nakatani, and Y. Shiratsuchi, Magnetic-field and temperature dependence of anomalous Hall effect in $\text{Pt}/\text{Cr}_2\text{O}_3/\text{Pt}$ trilayer, *AIP Advances* **12**, 035216 (2022).
- [29] Y. Cheng, S. Yu, M. Zhu, J. Hwang, and F. Yang, Evidence of the Topological Hall Effect in $\text{Pt}/\text{Antiferromagnetic Insulator Bilayers}$, *Physical Review Letters* **123**, 237206 (2019).
- [30] T. Moriyama, Y. Shiratsuchi, T. Iino, H. Aono, M. Suzuki, T. Nakamura, Y. Kotani, R. Nakatani,

- K. Nakamura, and T. Ono, Giant Anomalous Hall Conductivity at the Pt / Cr₂O₃ Interface, *Physical Review Applied* **13**, 034052 (2020).
- [31] S. Cao, M. Street, J. Wang, J. Wang, X. Zhang, C. Binck, and P. A. Dowben, Magnetization at the interface of Cr₂O₃ and paramagnets with large Stoner susceptibility, *Journal of Physics: Condensed Matter* **29**, 10LT01 (2017).
- [32] G. Kresse and J. Furthmüller, Efficient iterative schemes for *ab initio* total-energy calculations using a plane-wave basis set, *Physical Review B* **54**, 11169 (1996).
- [33] J. Hafner, *Ab-initio* simulations of materials using VASP: Density-functional theory and beyond, *Journal of Computational Chemistry* **29**, 2044 (2008).
- [34] P. E. Blöchl, Projector augmented-wave method, *Physical Review B* **50**, 17953 (1994).
- [35] P. Ziesche, S. Kurth, and J. P. Perdew, Density functionals from LDA to GGA, *Computational Materials Science* **11**, 122 (1998).
- [36] S. F. Sousa, P. A. Fernandes, and M. J. Ramos, General Performance of Density Functionals, *The Journal of Physical Chemistry A* **111**, 10439 (2007).
- [37] G. I. Csonka, J. P. Perdew, A. Ruzsinszky, P. H. T. Philipsen, S. Lebègue, J. Paier, O. A. Vydrov, and J. G. Ángyán, Assessing the performance of recent density functionals for bulk solids, *Physical Review B* **79**, 155107 (2009).
- [38] J. P. Perdew and A. Zunger, Self-interaction correction to density-functional approximations for many-electron systems, *Physical Review B* **23**, 5048 (1981).
- [39] D. M. Ceperley and B. J. Alder, Ground State of the Electron Gas by a Stochastic Method, *Physical Review Letters* **45**, 566 (1980).
- [40] V. I. Anisimov, J. Zaanen, and O. K. Andersen, Band theory and Mott insulators: Hubbard *U* instead of Stoner *I*, *Physical Review B* **44**, 943 (1991).
- [41] S. L. Dudarev, G. A. Botton, S. Y. Savrasov, C. J. Humphreys, and A. P. Sutton, Electron-energy-loss spectra and the structural stability of nickel oxide: An LSDA+*U* study, *Physical Review B* **57**, 1505 (1998).
- [42] S. Shi, A. L. Wysocki, and K. D. Belashchenko, Magnetism of chromia from first-principles calculations, *Physical Review B* **79**, 104404 (2009).
- [43] A. S. Kilian, G. J. Abreu, A. de Siervo, R. Landers, and J. Morais, Evidencing the formation of Pt nano-islands on Cr₂O₃/Ag(111), *CrystEngComm* **24**, 2270 (2022).
- [44] N. Shimomura, S. P. Pati, T. Nozaki, T. Shibata, and M. Sahashi, Enhancing the blocking temperature of perpendicular-exchange biased Cr₂O₃ thin films using buffer layers, *AIP Advances* **7**, 025212 (2017).
- [45] S. Fiori, D. Dagur, M. Capra, A. Picone, A. Brambilla, P. Torelli, G. Panaccione, and G. Vinai, Electronically ordered ultrathin Cr₂O₃ on Pt(111) in presence of a multidomain graphene intralayer, *Applied Surface Science* **613**, 155918 (2023).
- [46] I. Iino, T. Tada, K. Toyoki, R. Nakatani, and Y. Shiratsuchi, Anomalous Hall effect in Pt/Al-doped Cr₂O₃ epitaxial film, *AIP Advances* (2023).
- [47] X. Wang, K. Ujimoto, K. Toyoki, R. Nakatani, and Y. Shiratsuchi, Increase of Néel temperature of magnetoelectric Cr₂O₃ thin film by epitaxial lattice matching, *Applied Physics Letters* **121**, 182402 (2022).
- [48] T. V. A. Nguyen, Y. Shiratsuchi, A. Kobane, S. Yoshida, and R. Nakatani, Magnetic field dependence of threshold electric field for magnetoelectric switching of exchange-bias polarity, *Journal of Applied Physics* **122**, 073905 (2017).
- [49] A. Jain, S. P. Ong, G. Hautier, W. Chen, W. D. Richards, S. Dacek, S. Cholia, D. Gunter, D. Skinner, G. Ceder, and K. A. Persson, Commentary: The Materials Project: A materials genome approach to accelerating materials innovation, *APL Materials* **1**, 011002 (2013).
- [50] S. Bahn and K. Jacobsen, An object-oriented scripting interface to a legacy electronic structure code, *Computing in Science & Engineering* **4**, 56 (2002).
- [51] A. Hjorth Larsen, J. Jørgen Mortensen, J. Blomqvist, I. E. Castelli, R. Christensen, M. Dulak, J. Friis, M. N. Groves, B. Hammer, C. Hargus, E. D. Hermes, P. C. Jennings, P. Bjerre Jensen, J. Kermode, J. R. Kitchin, E. Leonhard Kolsbjerg, J. Kubal, K. Kaasbjerg, S. Lysgaard, J. Bergmann Maronsson, T. Maxson, T. Olsen, L. Pastewka, A. Peterson, C. Rostgaard, J. Schiøtz, O. Schütt, M. Strange, K. S. Thygesen, T. Vegge, L. Vilhelmsen, M. Walter, Z. Zeng, and K. W. Jacobsen, The atomic simulation environment—a Python library for working with atoms, *Journal of Physics: Condensed Matter* **29**, 273002 (2017).
- [52] A. Mahmoud, P.-M. Deleuze, and C. Dupont, The nature of the Pt(111)/ α -Fe₂O₃(0001) interfaces revealed by DFT calculations, *The Journal of Chemical Physics* **148**, 204701 (2018).
- [53] Z.-H. Zeng, J. L. F. Da Silva, H.-Q. Deng, and W.-X. Li, Density functional theory study of the energetics, electronic structure, and core-level shifts of NO adsorption on the Pt(111) surface, *Physical Review B* **79**, 205413 (2009).
- [54] P. Appel, B. J. Shields, T. Kosub, N. Hedrich, R. Hübner, J. Faßbender, D. Makarov, and P. Maletinsky, Nanomagnetism of Magnetoelectric Granular Thin-Film Antiferromagnets, *Nano Letters* **19**, 1682 (2019).
- [55] P. Makushko, T. Kosub, O. V. Pylypovskyi, N. Hedrich, J. Li, A. Pashkin, S. Avdoshenko, R. Hübner, F. Ganss, D. Wolf, A. Lubk, M. O. Liedke, M. Butterling, A. Wagner, K. Wagner, B. J. Shields, P. Lehmann, I. Veremchuk, J. Fassbender, P. Maletinsky, and D. Makarov, Flexomagnetism and vertically graded Néel temperature of antiferromagnetic Cr₂O₃ thin films, *Nature Communications* **13**, 6745 (2022).
- [56] P.-W. Ma and S. L. Dudarev, Constrained density functional for noncollinear magnetism, *Physical Review B* **91**, 054420 (2015).
- [57] A. L. Wysocki, S. Shi, and K. D. Belashchenko, Microscopic origin of the structural phase transitions at the Cr₂O₃ (0001) surface, *Physical Review B* **86**, 165443 (2012).
- [58] H. J. Xiang, E. J. Kan, S.-H. Wei, M.-H. Whangbo, and X. G. Gong, Predicting the spin-lattice order of frustrated systems from first principles, *Physical Review B* **84**, 224429 (2011).
- [59] We must mention that the rigorous quantitative accuracy of J_{ij} as obtained from Eq. 3 relies on the magnetic and electric properties of all atoms other than i and j remaining unchanged for the calculations. If this is the case, then $E(\theta = 0) - E(\theta = 180^\circ)$, which as shown in Fig. 4 is about 7 meV, should be precisely equal to $H_{\text{Heis}}^{\text{Cr12}, \theta=0} - H_{\text{Heis}}^{\text{Cr12}, \theta=180^\circ}$. However, using the values in Tab.II, we find that the difference between flipped and

antiferromagnetic configurations of Cr12 is 4.4 meV. The slight difference comes from the fact that in some of the configurations used in the 4-state method, specifically $E(\downarrow\uparrow)$, the Pt magnetization reverses (discussed in Sec. III C 2) with respect to its orientation in the three other magnetic configurations. Thus, our J values include a small contribution due to Cr_2O_3 –Pt interactions which does not cancel. However, the *relative* values of $J_{3,surf}$,

$J_{4,surf}$, and $J_{5,surf}$, which are what determines the energetic favorability of the flipped Cr_2O_3 configuration in the presence of Pt, should be reliable.

- [60] A. H. Hill, A. Harrison, C. Dickinson, W. Zhou, and W. Kockelmann, Crystallographic and magnetic studies of mesoporous eskolaite, Cr_2O_3 , Microporous and Mesoporous Materials **130**, 280 (2010).
- [61] J. W. Arblaster, Crystallographic Properties of Platinum, Platinum Metals Review **41** (1), 12 (1997).